Plasma jet acceleration of dust particles to hypervelocities

C. M. Ticoş,[1,2] Zhehui Wang,[1] G. A. Wurden,[1] J. L. Kline,[1] and D. S. Montgomery[1]
[1]*Los Alamos National Laboratory, Los Alamos, New Mexico 87545, USA*
[2]*National Institute for Laser, Plasma, and Radiation Physics, Bucharest 077125, Romania*

(Received 24 June 2008; accepted 12 September 2008; published online 6 October 2008)

A convenient method to accelerate simultaneously hundreds of micron-size dust particles to a few km/s over a distance of about 1 m is based on plasma drag. Plasma jets which can deliver sufficient momentum to the dust particles need to have speeds of at least several tens of km/s, densities of the order of 10^{22} m^{-3} or higher, and low temperature ~ 1 eV, in order to prevent dust destruction. An experimental demonstration of dust particles acceleration to hypervelocities by plasma produced in a coaxial gun is presented here. The plasma flow speed is deduced from photodiode signals while the plasma density is measured by streaked spectroscopy. As a result of the interaction with the plasma jet, the dust grains are also heated to high temperatures and emit visible light. A hypervelocity dust shower is imaged *in situ* with a high speed video camera at some distance from the coaxial gun, where light emission from the plasma flow is less intense. The bright traces of the flying microparticles are used to infer their speed and acceleration by employing the time-of-flight technique. A simple model for plasma drag which accounts for ion collection on the grain surface gives predictions for dust accelerations which are in good agreement with the experimental observations. © *2008 American Institute of Physics*. [DOI: 10.1063/1.2993229]

I. INTRODUCTION

Laboratory produced plasma flows are of interest for studying fundamental topics in plasma physics, such as, magnetohydrodynamic instabilities[1,2] and self-organization phenomena.[3] Plasma jets are also important in a number of applications which include surface processing,[4] refueling of fusion plasmas,[5,6] delivery of momentum flux in magnetized target fusion experiments,[7] or acceleration of dust particles to hypervelocities.[8,9] In this later case, the imparted momentum from the fast moving ions to the dust particles results in dust speeds of a few kilometers per second achieved in a time interval of only a few hundred microseconds.

Highly accelerated microparticles can be used in micrometeorite impact studies,[10,11] as a diagnostic tool for mapping the magnetic field vectors in fusion reactors,[12,13] or as a propulsion means for interplanetary flights.[14] Laboratory produced dusty-plasma flows can be of relevance in astrophysics, by simulating the conditions of stellar jets interaction with microparticle clouds.[15,16] Understanding of the ion drag force is an essential aspect of plasma-dust interaction.[17] For instance, the drag exerted by ion flow plays a key role in the formation of plasma crystals[18] or in the excitation of different dust acoustic waves.[19]

The plasma drag force exerted on microparticles is a subject of both theoretical and experimental investigation.[20–32] For grains much smaller than the plasma screening length ($r_d \ll \lambda_D$) and weak ion drift, the ion drag force can be deduced in the frame of the orbital-motion-limited (OML) theory.[33,34] Agreement between theoretical predictions for the ion drag and measurements has been obtained in experiments with free falling dust grains passing through a rf plasma,[27] in a dc plasma with subthermal ion drift,[28,29] suprathermal ion beam[30] or strong ion-dust coupling,[31] and in dust voids usually formed when the plasma is in microgravity conditions.[32] However, for the case of much smaller Debye length compared to the size of a microparticle ($r_d \gg \lambda_D$) experimental evidence of plasma drag dominating dust dynamics has been presented only recently.[8,9] Also, in this regime it is expected that the dust grains electrically charged by plasma are completely screened from each other and that the dust-dust Coulomb coupling is negligible. An object much larger than the Debye length rather describes the situation of Langmuir probes. From a shielding point of view however, electrical probes with sizes ≈ 1 mm immersed in weakly ionized gases, for which $\lambda_D \approx 0.1$ mm, can resemble dust grains or "miniature" probes of tens of microns present in cold (few eV) and dense plasmas ($n \gtrsim 10^{20}$ m^{-3}) with $\lambda_D \lesssim 1$ μm.[13]

The equilibrium or the slow motion of only a few mm/s of electrically charged dust grains immersed in low density plasmas ($\approx 10^{15}$ m^{-3}) is a feature useful for local diagnostics, such as, estimations of the sheath width or of the sheath electric fields.[35–39] It is a consequence of the interaction with the local electric fields, repulsion from the neighboring dust grains, gravitational pulling, friction with the neutral atoms, and drag exerted by ions. Depending on dust size and plasma parameters, ion drag can play an important role in the overall dust dynamics, especially for smaller dust grains.[29] The plasma environment where dust particles dragged by the plasma wind can reach speeds higher than 1–10 m/s requires plasma densities of at least 10^{19} m^{-3}, and sufficient ion flow speed.[8,9,13,40–44] Plasmas with these parameters can be produced in coaxial plasma guns[2,6,45,46] and can also be found at the edge of tokamak machines.[47–49]

There is an increased interest in dust laden dense plasmas present near the tokamak walls, motivated by the possible influence that dust can have on magnetically confined fusion plasmas.[40–43] Dust grains are usually detached from

the device walls as a result of the plasma-wall interactions and apparently migrate in the direction of the local plasma flow.[47,48] In the scrape-off-layer of tokamak plasma, hypervelocity dust moving at several km/s and colliding with electrostatic probe induced spikes in the signal recorded by the probe.[49,50] It is thought that dust formation and dust transport could pose a threat for the plasma sustainment itself or for the safety of operation[51,52] in the next-generation magnetic fusion devices, such as, ITER,[53] which are designed to operate over periods of several hundreds of seconds.

In this paper it is demonstrated that plasma drag exerted by cold (a few eV) and relatively dense (of the order of $n_i \gtrsim 10^{22}$ m^{-3}) plasma jets can simultaneously accelerate hundreds of micron-size dust grains to speeds up to a few km/s. The experiments are performed in deuterium plasma produced between two coaxial electrodes and expelled at about $\approx 25-60$ km/s by the $\mathbf{J}\times\mathbf{B}$ force. Here $\mathbf{J}$ is the radial current density between the electrodes and $\mathbf{B}$ is the azimuthal magnetic field generated by this current. The dust grains are from commercial dust powders made of graphite and diamond.

Plasma drag acceleration of dust particles has several advantages over other acceleration techniques. For instance, acceleration by compressed air can only deliver dust grains with speeds of a few hundred meters per second, limited by the sound speed of the gas. Linear electrostatic accelerators are a possible alternative for obtaining hypervelocity dust. However, besides the fact that their complex operation involves the use of megavolt power supplies, the acceleration is proportional to the charge accumulated on a dust grain. Charging of a dust grain is restricted by several factors such as grain size, field emission at the grain surface or the tensile strength of the dust material.

The paper is organized as follows: Sec. II presents the features of the plasma dynamic accelerator and the parameters of the ejected plasma flow. In Sec. III the optical system for dust detection and the measured dust acceleration are discussed. In Sec. IV the dust acceleration provided by a plasma drag model which accounts for direct collisions of ions with the grain is compared with the experimental results. Conclusions are drawn in Sec. V.

II. PLASMA DYNAMIC DUST ACCELERATOR

The plasma dynamic dust accelerator includes a coaxial plasma gun, an acceleration channel, a dust dispenser, and power and control devices, as shown in Fig. 1. The accelerator body is attached to a large vacuum tank with a diameter of 1.5 m and length of 4.5 m. The plasma gun consists of two electrodes: a center rod with 1.9 cm diameter and a coaxial cylinder with a 3.2 cm inner diameter, separated by a glass epoxy laminate ring. The length of the coaxial gap is 21 cm.[46]

A. Neutral gas pressure

Several root and turbomolecular pumps in the system create a base pressure of 3×10^{-6} Torr. For each fire sequence, deuterium gas is puffed for 1–4 ms at the middle of the gun by an electrically controlled Parker–Hanifin valve

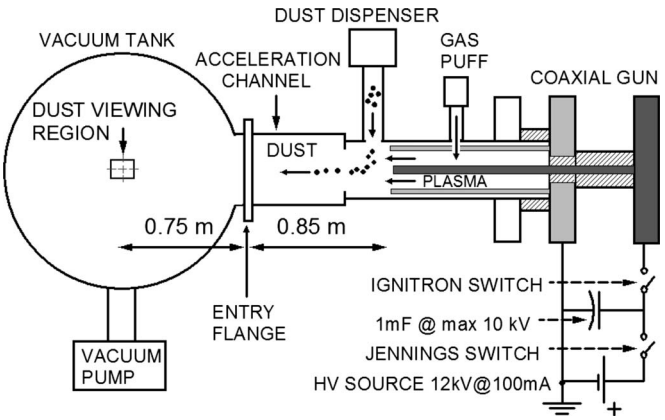

FIG. 1. Schematics of the coaxial plasma gun, dust dispenser, power circuit, and vacuum tank. The gun and dust dispenser are not to scale relative to the tank, however sizes are given for reference.

with a 1 ms opening time. A numerical analysis has been carried out to find out the instantaneous gas pressure in the system as a function of time. The valve is supplied with gas from a filled plenum. Since the pressure downstream from the small valve orifice with a diameter $d=0.8$ mm is much lower than that upstream (i.e., of the plenum), the valve is considered to work in a regime of chocked flow. For a small orifice, the gas throughput is[54]

$$Q_0 = c_0 P \frac{\pi d^2}{4}\sqrt{\frac{k_B T_g}{m_g}\frac{2\gamma}{\gamma+1}}\left(\frac{2}{\gamma+1}\right)^{(1/\gamma-1)}, \tag{1}$$

where c_0 is a coefficient that characterizes the contraction of the sonic gas flow ($c_0=0.85$), P is the upstream gas pressure, m_g is the mass of the gas atoms, and γ is the adiabatic coefficient of the gas. The puffed gas flows out of the coaxial gap and further expands into the acceleration channel and tank. The mean free path of the gas molecules for a range of pressures from 10^{-3} to 1 Torr is $\approx 10-0.01$ cm. We expect that for system compartments with larger volume, the pressure increase due to a determined mass of gas flowing in is lower. The Knudsen number for orifice diameters of 1–10 cm is 10^{-2} to 1. The gas flow is therefore in the intermediate regime, between molecular and viscous. For simplicity, we consider the flow in the molecular regime, with the throughput between the different vacuum compartments given by $Q=d(PV)/dt=C\Delta P$, where C is the conductance of an orifice and ΔP is the pressure difference on the sides of the orifice. $C=\bar{v}A/4$, where $\bar{v}=\sqrt{8k_BT_g/\pi m_g}$ is the average velocity of the gas particles and A is the area of the orifice. The length of the large tubular structures that make up the system brings a small contribution to the total conductance due to their relative large diameters and therefore it has been neglected. The evolution of gas pressure in time can be described by the following system of equations:

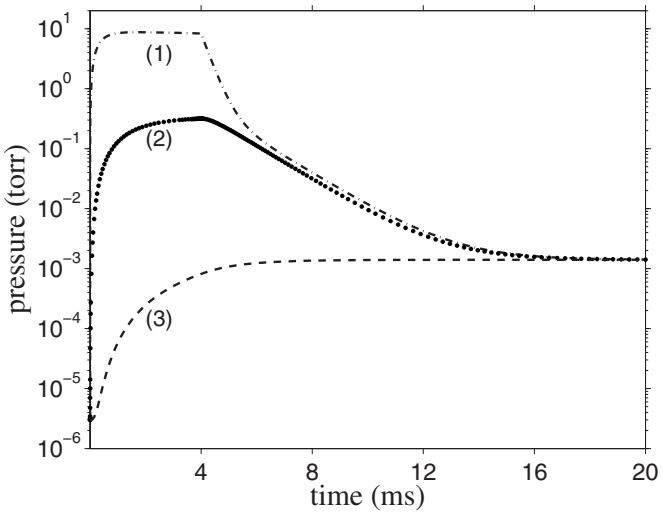

FIG. 2. Pressure variation in time from Eq. (2), during 4 ms gas-puff: curves (1), (2), and (3) show P_{gun}, P_{acc}, and P_{tank}, respectively.

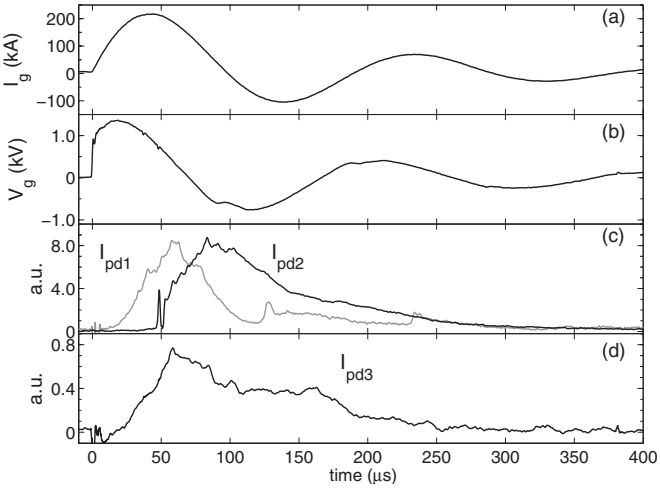

FIG. 3. Parameters of an 8 kV shot: gun current (a), voltage between electrodes (b), photodiode signals I_{pd1} and I_{pd2} with perpendicular view on the flow, and placed 0.9 m away from each other in (c), and signal from photodiode with end-on view inside the coaxial gap I_{pd3} in (d).

$$\frac{dP_{plen}}{dt} = -\frac{Q_0}{V_0},$$

$$\frac{dP_{gun}}{dt} = \frac{1}{V_g}[Q_0 - C_{esc}(P_{gun} - P_{acc})],$$

$$\frac{dP_{acc}}{dt} = \frac{1}{V_c}[C_{esc}(P_{gun} - P_{acc}) - C_t(P_{acc} - P_t)], \quad (2)$$

$$\frac{dP_t}{dt} = \frac{1}{V_t}[C_t(P_{acc} - P_t)],$$

where P_{plen}, P_{gun}, P_{acc}, and P_t are the pressures in the plenum, gun, acceleration channel, and tank, respectively, and $V_0=150$ cm^3, $V_g=115$ cm^3, $V_{acc}=0.012$ m^3, $V_t=7.068$ m^3 are their corresponding volumes. The conductance of the apertures between the four connected vacuum elements mentioned above are as follows: $C_0=3.83\times10^{-4}$, $C_{esc}=0.43$, and $C_t=7.85$ m^3/s. The plenum is filled at $P_{plen}=11.5$ atm. It is important to mention here that while the instantaneous pressure in these vessels is a function of both time and position, the time dependent pressure variables used in Eqs. (2) should be rather viewed as averages over the whole volume of each vessel and do not account for spatial distribution of the flow. The numerical solution of Eqs. (2) show that during gas puff the neutral gas pressure increases to 8 Torr in $\approx10^{-4}$ s within the interelectrode gap [curve (1) in Fig. 2] and to 0.2 Torr in ≈1 ms inside the acceleration channel [curve (2) in Fig. 2]. The pressure in the tank increases to 1.5 mTorr after 10 ms as shown in Fig. 2 with curve (3). While the solution of Eq. (2) can only provide an estimate for the exact pressure in the system, the predicted equilibrium pressure of 1–2 mTorr is in good agreement with the values measured by a time-averaged, slow response pressure gauge.

B. Electrical and optical characterization

The power circuit included a 1 mF capacitor bank, and a 12 kV @ 100 mA Glassman charging supply.[46] The system was remotely controlled from a computer by LabVIEW realtime software working on field-point modules. A commercial Pearson probe (10^{-3} V/A) with a rise time of 300 ns mounted around the high voltage end of the ignitron switch and coupled to two −20 dB attenuators was used to measure the instantaneous current. A Tektronix high-voltage probe measured the instantaneous voltage between the coaxial electrodes. An ignitron was used to close the circuit and initiate a discharge.

The characteristics of a 10 kV shot are shown in Fig. 3. The discharge current reaches its maximum value of 250 kA after ≈40 μs. During breakdown, the voltage drops in ≈5 μs to ≈1.8 kV. The underdamped current and voltage oscillations in the circuit are shown in Figs. 3(a) and 3(b). The speed of the bright plasma jet was deduced from optical measurements. A collimated photodiode I_{pd1} recorded the white light emitted at 0.25 m from the coaxial gun muzzle. A second photodiode (I_{pd2}) was placed downstream at a distance of 1.15 m from the gun muzzle and had also a side-view. Both photodiodes detected only light emitted in a solid angle $\approx5\times10^{-4}$ sr, perpendicular to the direction of the flow. From the time delay (16 ± 0.5 μs) between the peaks in their signals which are shown in Fig. 2(c), and the known distance between their locations (0.9 m), a plasma flow speed $v_f=56\pm2$ km/s can be estimated for a 10 kV shot. Measurements provided by a third photodiode with an end-on view which looked into the coaxial gap of the plasma gun indicate a total duration of the shot of ≈400 μs, Fig. 2(d). The parameters of a 6 kV and 8 kV shots are given in Table I. It is observed that the plasma flow speed increases with the energy delivered into the discharge. Images of the plasma jets that were ejected from the coaxial gun into the

TABLE I. Experimentally determined plasma flow speed, plasma density, and ion temperature for different discharge voltages and energy stored in the capacitor bank.

Voltage (kV)	Energy (kJ)	v_f(km/s)	$n_i(\times 10^{22}$ m$^{-3})$	Ti (eV)
6	18	26 ± 0.5	$0.2-1.5\pm0.1$	1.3 ± 0.3
8	32	38 ± 1	$0.5-2.2\pm0.1$	1.7 ± 0.4
10	50	56 ± 2	$0.5-3.1\pm0.2$	2.8 ± 0.7

tank are presented in Fig. 4. The images were captured by a high-speed camera (DiCam Pro, The Cooke Corp.) using a 16 mm f/4 fish eye lens.

C. Plasma parameters

The ion temperature was simply inferred from observations of the free expansion of the supersonic plasma flow into the vacuum tank, rather than by using line intensity ratios of excited plasma species. By knowing the axial flow speed from photodiode diagnostics, the plasma plume speed in a transversal direction could be found straightforwardly taking advantage of our high-speed imaging capabilities by measuring the expansion angle in the acquired pictures. If expanding ions are in thermal equilibrium and collisions with neutrals and recombination with electrons are neglected, the free expansion speed is roughly given by the ion thermal speed. The estimate provided by this method is sufficiently accurate for plasma jets produced in guns with similar electrode configurations, as shown in previous works.[6,10,11] The plasma temperatures of a few eV determined in this way agrees well with spectroscopic measurements.

If v_{Ti} is the thermal speed of ions, then we take $v_{Ti}\approx v_f\tan(\alpha)$, where α can be easily measured as shown in the image of Fig. 4(a): $\tan(\alpha)=0.29\pm0.05$, $v_f=56\pm2$ km/s, $v_{Ti}=16\pm3$ km/s, resulting in $T_i\approx2.8\pm0.7$ eV. For an 8 kV shot, the plume has a less elongated shape due to a lower axial flow speed, as seen in Fig. 4(b). For this shot, $\tan(\alpha)=0.34\pm0.06$, $v_f=38\pm1$ km/s, $v_{\rm th}=13\pm2.1$ km/s resulting in $T_i\approx1.7\pm0.4$ eV, while for a 6 kV shot the following values were obtained: $\tan(\alpha)=0.43\pm0.07$, $v_f=26\pm0.5$ km/s, $v_{\rm th}=11\pm1.7$ km/s, and $T_i\approx1.3\pm0.3$ eV, see Table I. In all presented cases, the plasma flow is supersonic, with Mach numbers between 3 and 4.

The plasma density as a function of time at a fixed location was determined from the Stark broadening of the D_α line using streaked spectroscopy. A lens with 5 cm diameter with a view perpendicular to the plasma flow was placed in front of a side window port of the acceleration channel, situated 25 cm from the gun muzzle. The lens collected the light emitted near the axis of the flow and focused it on an optical fiber coupled to a 0.5 m Chromex spectrometer provided with a 1800 lines/mm grating. The spectra were then passed to a Hamamatsu 4187 optical streak camera whose sweep unit time was set to 1 ms. The signals were recorded with a photometrics 250 scientific grade CCD camera with 1024×1024 pixels.

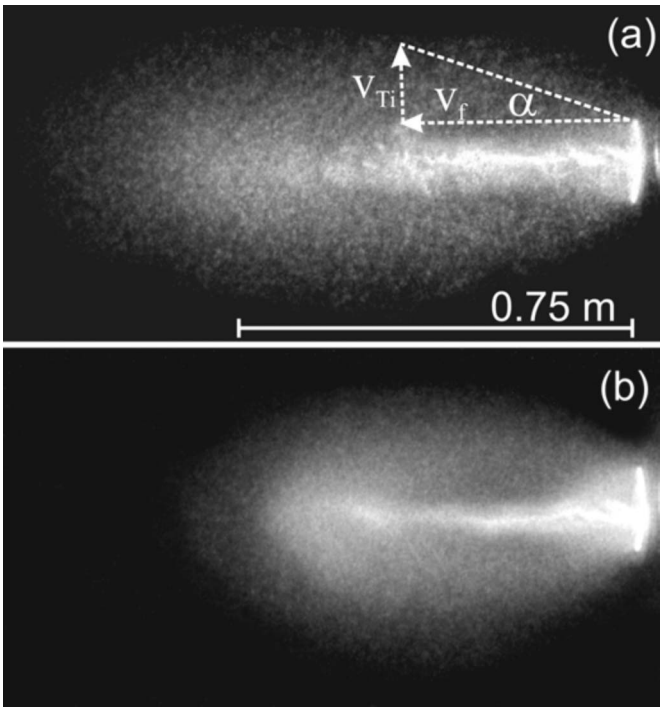

FIG. 4. Images of the plasma jet for a 10 kV shot and an exposure of 50 ns (a), and for an 8 kV shot and an exposure of 500 ns (b). The two pictures were acquired at 45 and 50 μs, respectively, from $t=0$. The tangent of the expansion angle α gives the ion thermal speed.

The measured D_α line is fitted with a Voigt profile which is given by the convolution of the plasma and instrument profile functions. The Voigt profile can be approximated by a linear combination of the two profile functions,[55]

$$I(\lambda)=(1-r)\frac{2\sqrt{\ln 2}}{\sqrt{\pi}w_V}\exp\left[-\frac{4\ln 2(\lambda-\lambda_0)^2}{w_V^2}\right]+r\frac{2}{\pi}\frac{w_L}{w_V^2+4(\lambda-\lambda_0)^2}, \quad (3)$$

where w_V is the full-width at half-maximum (FWHM) of the Voigt profile, and λ_0 is the D_α center line. $r=w_L/w_V$, where w_L and w_G are the FWHM of the Lorentzian and Gaussian profiles, respectively, and represents the weighting factor of these two profiles' contributions. The Lorentzian width can be deduced with sufficient accuracy as a function of the Voigt and Gaussian widths, $w_L\cong w_V-w_G/w_V^2$. w_V is the measured width of the plasma profile and w_G is the instrument width which was determined from calibrations using a pen lamp.

The ion density is inferred from the FWHM of the plasma profile, $w_L=0.54\ \alpha_{1/2}\ n_i^{2/3}$ (nm),[56] where $\alpha_{1/2}\approx0.01$,[57] and n_i is the ion density in units of 10^{20} m^{-3}. In Fig. 5 the profiles of the D_α line at two different moments during a 10 kV shot are shown. Curve (1) was acquired at $t=75$ μs from $t=0$ of the discharge and curve (2) at 90 μs. The Lorentzian widths of these profiles with $w_{V1}=1.6$ Å and $w_{V2}=2.5$ Å are obtained by accounting for the instrument width $w_G=0.8$ Å: $w_{L1}=1.2$ Å and $w_{L2}=2.2$ Å. The calculated plasma densities resulting from these two fits are $n_i\approx1$ and 2.7×10^{22} m^{-3}, respectively. The plasma density is

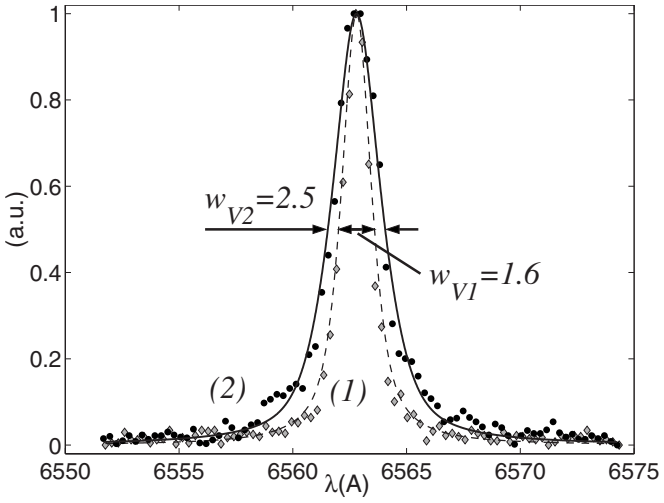

FIG. 5. Measured D_α (λ_0=6562.8 Å) profiles for a 10 kV shot at different moments in time: $t \simeq 75$ μs (diamonds) and $t \simeq 90$ μs (dots). The fitted curves (1) and (2) shown with continuous/dashed lines represent a Voigt profile, given by Eq. (3).

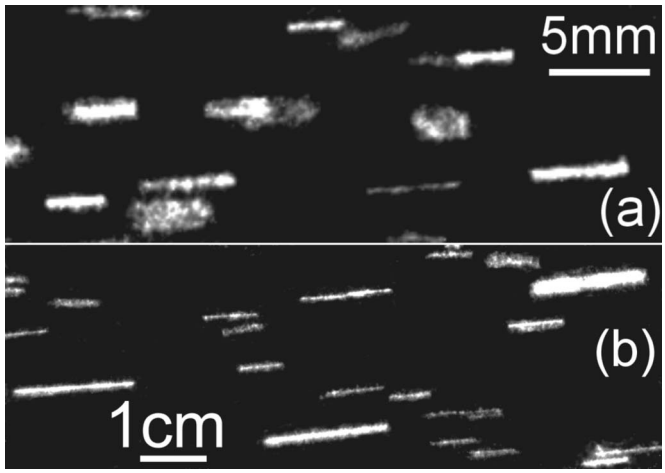

FIG. 6. Self-glowing grains made of diamond (a) and graphite (b), flying at 1.6 m from the gun muzzle. The exposure time is 4 μs and 12 μs, for (a) and (b). The shown images are small cuts of about 300×100 pixels from the full recorded pictures of 1280×1024 pixels.

not constant during a shot; it varies in time within the ranges given in Table I, which depend on the discharge voltage. Our diagnostic technique provides the average plasma density over the whole cross section of the flow. The lower density layer at the flow edge may in fact reduce the width of the observed line.[57]

Bright plasma filaments originating inside the plasma dynamic accelerator and extended over most of the plasma plume length are clearly visible in Figs. 4(a) and 4(b). Their presence suggest there are regions in the cross section of the flow where plasma density is higher, possibly due to the pinch effect which can lead to a peaked density on the axis of the plasma flow. Thus, the values presented in Table I could be lower than the actual density at the center of the plasma column. The plasma filaments occur naturally during each shot. Their structure cannot be predicted nor controlled, by changing the discharge parameters.

III. DETECTION AND MEASUREMENT OF HYPERVELOCITY DUST GRAINS

Synthetic diamond powder with particle radii $20 \leqslant r_d \leqslant 30$ μm and density ρ_d=3.52 g/cm^3 and graphite powder with a large range of sizes $0.5 \leqslant r_d \leqslant 24$ μm and density ρ_d=2.24 cm^{-3}, both manufactured by Alfa Aesar, were used in the experiment. The dust dispenser was an aluminium cylinder under vacuum which hosted a dust cup. It was shaken by a 28 kHz piezo-transducer, mounted at its top.[46] The grains were released continuously in front of gun the muzzle while a shot was fired.

Dust acceleration to hypervelocities is demonstrated by in-flight observations of grains flying at several km/s. The total number of moving grains identified in all our recorded images is approximately 1.94×10^3. A Sigma telephoto lens with 500 mm f/4 and magnification M 1:5.2, mounted on the DicamPro camera, was focused onto a small region of about 11×14 cm situated downstream of the plasma flow at 1.6 m from the gun muzzle. For optimal viewing purposes this region was chosen to be on the axis of the cylindrical vacuum tank and far enough from the gun muzzle to avoid the intense plasma light emission. The camera positioned about 2 m away from the observation region was looking almost perpendicularly (~80°) on the flow direction. Ahead of the experiment, a rod provided with a fine vertical ruler was positioned in the observation region, and was used for calibrating the images recorded by the camera.

The optical system which includes the CCD of the high-speed camera and the telephoto lens could only resolve grains with radii of at least 5 μm.[8] The minimum detectable dust radius r_d can be found based on its image size and the detection optics,[58,59] $r_d = \sqrt{d_e^2 - d_s^2}/2M$, where $d_s = 2.44(1+M)\lambda f\#$ is the diffraction-limited spot diameter for the camera with $f\#$ (=4 for the telephoto lens), and M=0.19. The wavelength has been chosen at the middle of the visible spectrum, λ=550 nm. The ICCD detector of the DiCaM Pro camera has a pixel size of 6.7×6.7 μm, therefore d_e=6.7 μm.

A wide range of time delays relative to the plasma ignition time, between 100 and 3×10^3 μs, has been scanned with our high-speed camera, in order to detect hypervelocity dust. The exposure time was set for 2–16 μs. The accelerated dust grains emitted visible light due to the intense heating by the plasma particle fluxes and appeared as glowing tracers, as shown in Fig. 6. Their speed was inferred by using the time-of-flight technique, from the ratio between the length of their trace and the exposure time of the image. Flying diamond (a) and graphite (b) grains are shown in Fig. 6. The exposure times are 4 μs for image (a) and 12 μs for image (b). The speed of the pictured diamond grains is therefore in the range 0.8–1.5 km/s. The graphite grains have similar speeds, between 0.4 and 1.5 km/s. Their longer traces are compensated by the longer image exposure. While the mass density and size of the grains shown is different for the two pictures, their comparable speed is due to differences in the flow speed and plasma density, and therefore in the drag force: (a) is for a 10 kV shot while (b) for a 6 kV shot.

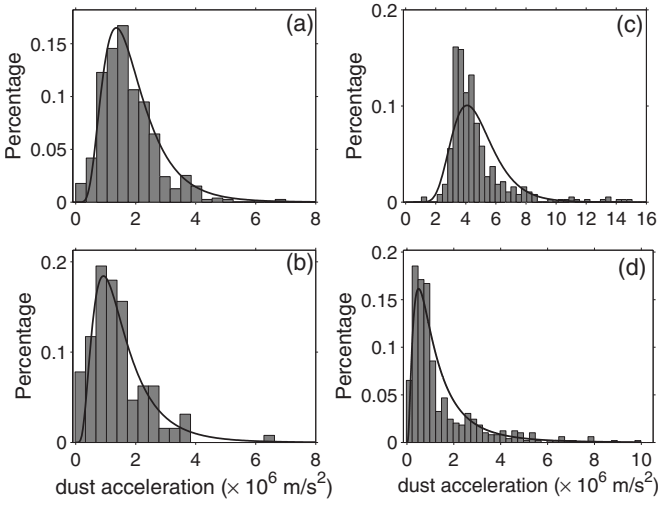

FIG. 7. Dust acceleration for diamond dust in the case of 10 kV shots (a) and 8 kV shots (b); dust acceleration for graphite dust in the case of 8 kV shots (c) and 6 kV shots (d). A log-normal fit is shown with a continuous line.

The pictures of Fig. 6 also show traces of different thickness, which can be divided into two categories: On the one hand, there are well resolved traces with different widths situated in the focusing region of the lens, while on the other hand there are traces with a blurred aspect and an apparent thickness comparable to their length. In this later case, the traces are thought to be situated at the edge of the field of view, which for our optical setup was about 4 cm, and could not be clearly resolved. While in the first case, the trace widths are proportional with the grain sizes, in the second case the trace appearance is only an optical effect.

Dust acceleration is achieved in two stages, corresponding to neutral gas drag followed by plasma drag. Neutral gas drag is at least one order of magnitude lower than plasma drag in our experiment, as it will be shown in the next section. The dynamics of dust particles due to neutral drag has not been observed experimentally, but only simulated using a gas drag model.[17] The effect of the neutral gas drag on dust is transport in the axial direction, depending on the grains size and their mass. The dust particles are displaced to some distance from the gun muzzle, which vary from 1 cm to several tens of centimeters, when the plasma is fired. In the overall dust dynamics the neutral gas drag force has a negligible contribution to grain acceleration. It is too small to produce a visible difference in the hypervelocity dust trajectories. We attempted to observe only neutral-gas dragged dust particles for a wide range of puffed gas pressures, but none have been detected.

Acceleration due to plasma drag is inferred from the ratio of dust speed to the plasma duration time (400 μs), or to the trigger time of the camera from $t=0$, if the dust traces were recorded at shorter times. For instance, a small number of dusts were detected in images acquired as soon as 180 μs from plasma firing. The results are presented in Fig. 7. For 10 kV shots, most of the diamond grains have accelerations within $1-3\times10^6$ m/s^2, while for 8 kV shots the bulk of grain accelerations is situated within the range $5\times10^5-2.5\times10^6$ m/s^2. For graphite dust the difference in dust acceleration for two plasma regimes is even more pronounced. For 8 kV shots, most of the grains have $2.5-7\times10^6$ m/s^2, while in the case of 6 kV shots a large number of grains have $5\times10^5-3.5\times10^6$ m/s^2. Occasionally, a small percentage of dust grains with accelerations of $7-15\times10^6$ m/s^2 can be seen in all recorded shots. Dust acceleration is higher for denser plasma with larger flow speed and for lighter dust particles which have less inertia, as expected.

From the plots we observe that each data set presented in Fig. 7 can be fitted by a log-normal distribution,

$$P_d = \frac{1}{a_d\sigma\sqrt{2\pi}}\exp\left\{-\frac{[\ln(a_d)-\mu]^2}{2\sigma^2}\right\}, \tag{4}$$

where μ and σ are the mean and standard deviation, respectively, of $\ln(a_d)$. The goodness of each fit is checked using the Anderson–Darling test.[60] The distribution parameters are $\mu_1=14.02$, $\sigma_1=0.61$, and $\mu_2=14.54$, $\sigma_2=0.49$, for the 8 and 10 kV, respectively, for diamond dust. For graphite dust and the shots corresponding to 6 and 8 kV, $\mu_3=13.86$, $\sigma_3=0.86$, and $\mu_4=15.33$, $\sigma_4=0.32$, respectively.

The fitting technique is particularly useful as it provides us with a simple tool for assessing some statistical properties of the measured data. Thus, the confidence intervals of this distribution give an estimate of the most probable dust acceleration within the bulk data. The boundaries of these confidence intervals depend on the geometric mean $\exp(\mu)$ and on the geometric standard deviation $\exp(\sigma)$. About 67% of the samples are expected to be situated in the interval $[\exp(\mu-\sigma)\exp(\mu+\sigma)]$, which for the data presented in Figs. 7(a)–7(d) is as follows, in units of 10^6 m/s^2: [1 2.8], [0.7 2.4], [3.2 4.1], and [0.4 3.3]. It can be clearly seen how the range of measured dust acceleration shifts towards higher values for increased flow speed and plasma density, and also the peak in the distribution follows the same trend.

IV. SIMULATION OF DUST ACCELERATION BY NEUTRAL AND PLASMA DRAG FORCES

The drag force exerted by the neutral gas flowing with its thermal speed well before pressure equilibration in the system is given by $8/3\sqrt{2\pi}r_d^2P_n\xi$, where P_n is the neutral gas pressure and $\xi(=1.5)$ is a factor which accounts for diffuse reflection of neutrals on the grain surface.[17] The pressure distribution in the acceleration channel is approximated with a function which decreases linearly with distance, from 8 Torr at the gun muzzle to 0.2 Torr at the end (0.85 m) of the acceleration channel, during the gas-puff period which is the interval [0 1] ms. The dust acceleration resulted from neutral gas drag is presented in Figs. 8(a) and 8(c) with the dashed-dotted line. Diamond dust and large ($r_d=22$ μm) graphite grains can only be pushed by the neutral gas flow with accelerations $\simeq 2-3\times10^4$ m/s^2 due to their relatively high mass, however, small graphite particles ($r_d=5$ μm) can reach about 2×10^5 m/s^2. During gas puff the dust temperature remains constant, as shown in Figs. 8(b) and 8(d).

A simulation for plasma drag which accounts for dust heating by plasma particles, vaporization at the dust surface and change in dust radius, thermionic and secondary emis-

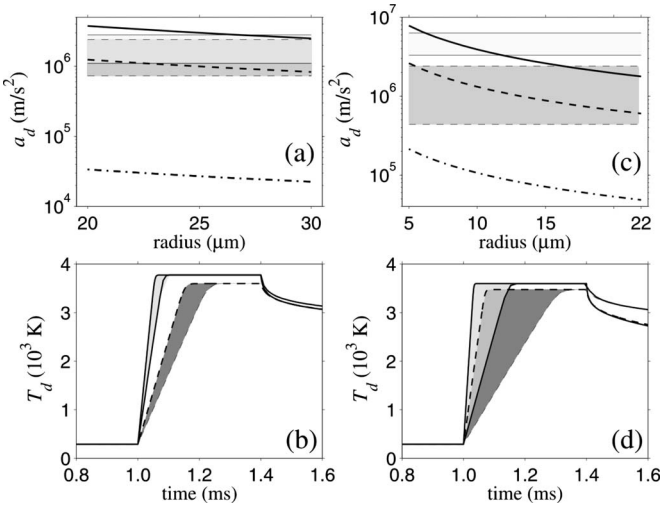

FIG. 8. Simulations for diamond dust in (a) and (b) and graphite dust in (c) and (d). (a) Curves $a_d(r_d)$ for a 10 kV shot (-), 8 kV shot (- -), and for neutral gas drag (- ·). The two bands (-) and (- -) are the experimental results for the two regimes. In (b) the light grey area corresponds to a 10 kV shot, while the dark grey area is for an 8 kV shot. Both areas correspond to grains with r_d=20 μm (the upper bound) to r_d=30 μm (the lower bound); (c) curves $a_d(r_d)$ for an 8 kV shot (-), 6 kV shot (- -), and for neutral gas drag (- ·). The two bands (-) and (- -) are the experimental results for the two regimes. In (d) the light and dark grey areas correspond to 8 kV and 6 kV shots, respectively. They describe the grains with sizes from r_d=5 μm (the upper bound) to r_d=22 μm (the lower bound). The overlapping region is shown with medium dark grey.

sion, and radiative cooling is performed to explain dust acceleration to hypervelocities. For our plasma parameters $\lambda_D \approx 10^{-7}$ m $\ll r_d$. Thus, the plasma screening length is much smaller than the grain sizes. The electron and ion currents to the dust surface are deduced in the sheath limited theory, supposing that a thin sheath surrounds the grain. The electron current depends on the dust potential V_d ($V_d<0$) through the Boltzmann distribution while the ion current is proportional with the supersonic plasma flow speed v_f rather than the ion sound speed,

$$I_e = 2\pi r_d^2 e n_e \sqrt{\frac{k_B T_e}{2\pi m_e}} \exp\left(\frac{eV_d}{k_B T_e}\right), \tag{5}$$

$$I_i = 2\pi r_d^2 e n_i v_f. \tag{6}$$

The electron and ion temperatures and densities are assumed equal in the simulation. The equilibrium dust charge is reached when there is no net current to the dust surface: $0=I_i+I_e+I_{\text{therm}}+I_{\text{sec}}$. Here I_{therm} and I_{sec} are the thermionic and secondary electron emission currents, given in Ref. 44. Heating of a dust particle is due to the plasma ions and electrons, which deposit their kinetic energy on the dust surface. The corresponding heat fluxes are given in Ref. 44.

The equation of motion for a plasma-dragged spherical grain is[61]

$$m_d \frac{v_d}{dt} = 2\pi r_d^2 k_B T_i n_i G_0(s) \equiv F_c,$$

where $s=[m_i(v_f-v_d)^2/2k_BT_i]^{1/2}$, and

$$G_0(s) = \left(s^2 + 1 - \frac{1}{4s^2}\right)\text{erf}(s) + \left(s + \frac{1}{2s}\right)\frac{\exp(-s^2)}{\sqrt{\pi}}. \tag{7}$$

In the model, only direct collisions of plasma ions with the grain contribute to the drag force. Electron drag is neglected due to low electron mass. m_d is the mass of a grain, v_d is the grain speed, m_i is the ion mass, n_i and T_i are the ion density and temperature. The equations for temperature, dust radius and charge variation in time are solved simultaneously with the equation of motion. The flow speed and plasma temperature are given in Table I. The plasma density is taken to be constant and equal with the largest values shown in Table I for the three cases considered in the experiment: 6, 8, and 10 kV shots.

The acceleration as a function of dust radius is shown in Figs. 8(a) and 8(c). For diamond dust $a_d \simeq \sim 2.5-4 \times 10^6$ m/s^2 for a 10 kV shot and $\simeq 8\times 10^5 - 1.5\times 10^6$ m/s^2 for an 8 kV shot. In the case of graphite grains the large distribution of sizes results in a wider range of accelerations, from 2 to 9×10^6 m/s^2 for an 8 kV shot and from 6×10^5 to 2.5×10^6 m/s^2 for a 6 kV shot. The acceleration due to plasma drag can be up to two orders of magnitude higher than neutral gas drag.

The predicted dust accelerations are within the ranges of the measured ones, for which the confidence intervals are shown with horizontal gray bands in Fig. 8. A small percentage of faster or slower moving dust grains can be observed in the experiment, see Fig. 7, as compared to the simulations. While in the model the plasma density is taken constant, in the experiment the flow is not homogeneous. The filamentary structures observed in the plasma flow of Fig. 4 are believed to be associated with plasma density gradients, which can lead to a wider distribution of dust accelerations.

In the experiment no external magnetic fields are applied. The inductive electric fields are estimated using Ampere and Faraday laws and the measured discharge currents. The azimuthal magnetic field near the center electrode is $B_\varphi(t)=\mu_0 I(t)/2\pi r$; the electric field is inferred from $\partial E_r/\partial z - \partial E_z/\partial r = -\partial B_\varphi/\partial t$. Here r means the radial direction, and z is along the electrodes axis. The radial component E_r is perpendicular to the dust motion and therefore it does not bring any contribution to the dust acceleration. For a sinusoidal current profile in time $\partial E_z/\partial r \simeq \omega \sin(\omega t)\mu_0 I/2\pi r$, and therefore $E_{z\,\max} \simeq \omega \ln(r/a)\mu_0 I_{\text{peak}}/2\pi$, where a is the radius of the center rod. For our experiment $I_{\text{peak}} \simeq 250$ kA, $\omega \simeq 3\times 10^4$ Hz, $r/a \simeq 2$, and $E_{z\,\max} \lesssim 10$ V/cm. The electrostatic field is also in the radial direction and is not affecting axial dust motion. The equilibrium dust potential found numerically is $\sim -1.5kT_e$. By taking the charge on a dust grain $Q_d \simeq 4\pi\varepsilon_0 r_d^2 V_d$, it is found that the electrostatic force $Q_d E$ in the flow direction is many orders of magnitude smaller than F_c. Also, the charge on the grain remains negative in spite of thermionic emission which becomes important at high dust temperatures.[62]

During the interaction with the plasma flow, i.e., the interval [1 1.4] ms in our simulation, the grain temperature increases abruptly to above 3000 K for both types of dusts [Figs. 8(b) and 8(d)]. The temperature reaches a plateau at 3550–3750 K, where the incoming heat flux of ions and

electrons is equilibrated mostly by the outgoing heat flux of vaporization. In this regime the dust radius decreases in time at a rate which depends on plasma parameters, initial grain size, and dust material. Thus, in the plasma flow of a 10 kV shot, a diamond grain with $r_d=20\ \mu$m diminishes with 5%/ms, while 80% of a graphite grain with $r_d=10\ \mu$m is vaporized after about 400 μs. For a 6 kV shot heating is slower for a large graphite grain with $r_d=22\ \mu$m, as demonstrated by the dashed line in Fig. 8(d), which bounds the dark grey area. After 1.4 ms, when the plasma-dust interaction ends, radiative cooling $\propto\sigma(T_d^4-T_{\mathrm{wall}}^4)$ ($T_{\mathrm{wall}}=290$ K) leads to a slow decay of the dust temperature. Partial destruction of the grains due to short exposure to plasma is predicted in the simulation. In the present experiment however, the degree of dust vaporization is not measured. An analysis of the structure and size of the grains that are left after the interaction with the dense plasma flow is deferred for future work.

V. CONCLUSIONS

An experimental demonstration of dust particles acceleration to several km/s by cold and dense plasma flows is presented. Deuterium gas and carbon grains have been chosen for compatibility with fusion plasmas. A good agreement is found between the experimental results and the predictions of a plasma drag model for dust acceleration based on direct collision of ions with the grain. Also heating of dust particles by the plasma fluxes to high temperatures in the simulation is confirmed by the self-luminous appearance of the flying grains, a feature that is helpful for *in situ* dust imaging. This plasma-based dust acceleration technique has several key features. It can use any type of gas and it can effectively work for hundreds of dust grains at the same time. Also the dust grains can have a large size distribution, from 1 to several tens of microns in radius, and in principle can have any shape. The dust material requires a relatively high temperature melting point, to minimize vaporization of the grains during plasma acceleration.

ACKNOWLEDGMENTS

The authors wish to acknowledge illuminating discussions with Professor P. K. Shukla.

This work was supported in part by the U.S. Department of Energy, under Contract No. DE-AC52-06NA25396, through the Office of Science, and by the Romanian National University Research Council (CNCSIS) under Contract No. RP-10, within the PNCDI2 program.

[1] I. Furno, T. P. Intrator, G. Lapenta, L. Dorf, S. Abbate, and D. D. Ryutov, Phys. Plasmas **14**, 022103 (2007).
[2] U. Shumlak, R. P. Golingo, B. A. Nelson, and D. J. D. Hartog, Phys. Rev. Lett. **87**, 205005 (2001).
[3] S. C. Hsu and P. M. Bellan, Phys. Plasmas **12**, 032103 (2005).
[4] K. F. Schoenberg, R. A. Gerwin, R. W. Moses, Jr., J. T. Scheuer, and H. P. Wagner, Phys. Plasmas **5**, 2090 (1998).
[5] P. B. Parks, Phys. Rev. Lett. **61**, 1364 (1988).
[6] V. Voronin, V. K. Gusev, Yu. V. Petrov, N. V. Sakharov, K. B. Abramova, E. M. Sklyarova, and S. Yu. Tolstyakov, Nucl. Fusion **45**, 1039 (2005).
[7] Y. C. F. Thio, C. E. Knapp, R. C. Kirkpatrick, R. E. Siemon, and P. J. Turchi, J. Fusion Energy **20**, 1 (2001).
[8] Z. Wang, C. M. Ticos, and G. A. Wurden, Phys. Plasmas **14**, 103701 (2007).
[9] C. M. Ticos, Z. Wang, G. A. Wurden, J. L. Kline, D. S. Montgomery, L. A. Dorf, and P. K. Shukla, Phys. Rev. Lett. **100**, 155002 (2008).
[10] E. B. Igenbergs and E. L. Shriver, J. Appl. Phys. **44**, 2177 (1973).
[11] A. Hüdepohl, M. Rott, and E. Igenbergs, IEEE Trans. Magn. **25**, 232 (1989).
[12] Z. Wang and G. A. Wurden, Rev. Sci. Instrum. **74**, 1887 (2003).
[13] Z. Wang, C. M. Ticos, L. A. Dorf, and G. A. Wurden, IEEE Trans. Plasma Sci. **34**, 242 (2006).
[14] K. Avinash and G. P. Zank, Phys. Plasmas **14**, 053507 (2007).
[15] C. K. Goertz, Rev. Geophys. **27**, 271, DOI: 10.1029/RG027i002p00271 (1989).
[16] A. L. Graps, E. Grün, H. Svedhem, H. Krüger, M. Horányi, A. Heck, and S. Lammers, Nature (London) **405**, 48 (2000).
[17] P. K. Shukla and A. A. Mamun, *Introduction to Dusty Plasma Physics* (IOP, Bristol, 2002).
[18] H. M. Thomas and G. E. Morfill, Nature (London) **379**, 806 (1996).
[19] P. K. Shukla and V. P. Silin, Phys. Scr. **45**, 508 (1992).
[20] M. S. Barnes, J. H. Keller, J. C. Forster, J. A. O'Neill, and D. Keith Coultas, Phys. Rev. Lett. **68**, 313 (1992).
[21] M. D. Kilgore, J. E. Daugherty, R. K. Porteous, and D. B. Graves, J. Appl. Phys. **73**, 7195 (1993).
[22] S. A. Khrapak, A. V. Ivlev, G. E. Morfill, and H. M. Thomas, Phys. Rev. E **66**, 046414 (2002).
[23] S. A. Khrapak, A. V. Ivlev, S. K. Zhdanov, and G. E. Morfill, Phys. Plasmas **12**, 042308 (2005).
[24] A. V. Ivlev, S. A. Khrapak, S. K. Zhdanov, G. E. Morfill, and G. Joyce, Phys. Rev. Lett. **92**, 205007 (2004).
[25] V. N. Tsytovich, U. de Angelis, A. V. Ivlev, G. E. Morfill, and S. Khrapak, Phys. Plasmas **12**, 112311 (2005).
[26] I. H. Hutchinson, Plasma Phys. Controlled Fusion **48**, 185 (2006); **47**, 71 (2005).
[27] C. Zafiu, A. Melzer, and A. Piel, Phys. Plasmas **10**, 1278 (2003).
[28] S. Ratynskaia, S. Khrapak, A. Zobnin, M. H. Thoma, M. Kretschmer, A. Usachev, V. Yaroshenko, R. A. Quinn, G. E. Morfill, O. Petrov, and V. Fortov, Phys. Rev. Lett. **93**, 085001 (2004).
[29] V. Yaroshenko, S. Ratynskaia, S. Khrapak, M. H. Thoma, M. Kretschmer, H. Höfner, G. E. Morfill, A. Zobnin, A. Usachev, O. Petrov, and V. Fortov, Phys. Plasmas **12**, 093503 (2005).
[30] M. Hirt, D. Block, and A. Piel, Phys. Plasmas **11**, 5690 (2004).
[31] V. Nosenko, R. Fisher, R. Merlino, S. Khrapak, G. Morfill, and K. Avinash, Phys. Plasmas **14**, 103702 (2007).
[32] M. Kretschmer, S. A. Khrapak, S. K. Zhdanov, H. M. Thomas, G. E. Morfill, V. E. Fortov, A. M. Lipaev, V. I. Molotkov, A. I. Ivanov, and M. V. Turin, Phys. Rev. E **71**, 056401 (2005).
[33] J. E. Allen, Phys. Scr. **45**, 497 (1992).
[34] M. Lampe, J. Plasma Phys. **65**, 171 (2001).
[35] E. B. Tomme, D. A. Law, B. M. Annaratone, and J. E. Allen, Phys. Rev. Lett. **85**, 2518 (2000).
[36] A. A. Samarian and B. W. James, Phys. Lett. A **287**, 125 (2001).
[37] C. M. Ticos, A. Dyson, and P. W. Smith, Plasma Sources Sci. Technol. **395**, 402 (2004).
[38] E. Thomas, Jr. and J. Williams, Phys. Rev. Lett. **95**, 055001 (2005).
[39] T. E. Sheridan, M. R. Katschke, and K. D. Wells, Rev. Sci. Instrum. **78**, 023502 (2007).
[40] S. I. Krasheninnikov, Y. Tomita, R. D. Smirnov, and R. K. Janev, Phys. Plasmas **11**, 3141 (2004).
[41] A. Yu. Pigarov, S. I. Krasheninnikov, T. K. Soboleva, and T. D. Rognlien, Phys. Plasmas **12**, 122508 (2005).
[42] R. D. Smirnov, A. Yu. Pigarov, M. Rosenberg, S. I. Krasheninnikov, and D. A. Mendis, Plasma Phys. Controlled Fusion **49**, 347 (2007).
[43] Y. Tanaka, A. Yu. Pigarov, R. D. Smirnov, S. I. Krasheninnikov, N. Ohno, and Y. Uesugi, Phys. Plasmas **14**, 052504 (2007).
[44] C. M. Ticos, Z. Wang, G. L. Delzanno, and G. Lapenta, Phys. Plasmas **13**, 103501 (2006).
[45] Z. Wang, P. D. Beinke, C. W. Barnes, M. W. Martin, E. Mignardot, G. A. Wurden, S. C. Hsu, T. P. Intrator, and C. P. Munson, Rev. Sci. Instrum. **76**, 033501 (2005).
[46] C. M. Ticos, Z. Wang, L. A. Dorf, and G. A. Wurden, Rev. Sci. Instrum. **77**, 10E304 (2006).
[47] A. L. Roquemore, W. Davis, R. Kaita, C. H. Skinner, R. Maqueda, and N. Nishino, Rev. Sci. Instrum. **77**, 10E526 (2006).
[48] D. L. Rudakov, W. P. West, C. P. C. Wong, N. H. Brooks, T. E. Evans, M. E. Fenstermacher, M. Groth, S. I. Krasheninnikov, C. J. Lasnier, A. G.

McLean, A. Yu. Pigarov, W. M. Solomon, G. Y. Antar, J. A. Boedo, R. P. Doerner, E. M. Hollmann, A. W. Hyatt, R. A. Moyer, and J. G. Watkins, J. Nucl. Mater. **363–365**, 227 (2007).
[49]C. Castaldo, S. Ratynskaia, V. Pericoli, U. de Angelis, K. Rypdal, L. Pieroni, E. Giovannozzi, G. Maddaluno, C. Marmolino, A. Rufoloni, A. Tuccillo, M. Kretschmer, and G. E. Morfill, Nucl. Fusion **47**, L5 (2007).
[50]S. Ratynskaia, C. Castaldo, K. Rypdal, G. Morfill, U. de Angelis, V. Pericoli-Ridolfini, A. Rufoloni, and A. Giovannozzi, Nucl. Fusion **48**, 015006 (2008).
[51]J. Winter, Plasma Phys. Controlled Fusion **46**, B583 (2004).
[52]M. Rubel, M. Cecconello, J. A. Malmberg, G. Sergienko, W. Biel, J. R. Drake, A. Hedqvist, A. Huber, and V. Philipps, Nucl. Fusion **41**, 1087 (2001).
[53]J. P. Sharpe, D. A. Petti, and H.-W. Bartels, Fusion Eng. Des. **63–64**, 153 (2002).
[54]J. F. O'Hanlon, *A User's Guide to Vacuum Technology* (Wiley, New York, 1989).
[55]E. E. Whiting, J. Quant. Spectrosc. Radiat. Transf. **8**, 1379 (1968).
[56]I. H. Hutchinson, *Principles of Plasma Diagnostics* (Cambridge University Press, Cambridge, 2002).
[57]H. R. Griem, *Spectral Line Broadening by Plasmas* (Academic, New York, 1974).
[58]R. J. Adrian, Appl. Opt. **23**, 1690 (1984).
[59]M. Raffel, C. Willert, and J. Kompenhans, *Particle Image Velocimetry: A Practical Guide* (Springer-Verlag, Berlin, 2002), pp. 38–40.
[60]http://www.mathwave.com/products/easyfit.html, Mathwave Technologies, Topol 3, 30/2/27 Dnepropetrovsk, 49041 Ukraine.
[61]B. T. Draine and E. E. Salpeter, Astrophys. J. **231**, 77 (1979).
[62]G. L. Delzanno, G. Lapenta, and M. Rosenberg, Phys. Rev. Lett. **92**, 035002 (2004).